

Assessment of gas and liquid velocities induced by an impacting liquid drop

B.H. Bang^a, S.S. Yoon^{a,*}, H.Y. Kim^a, S.D. Heister^b, H. Park^c, S.C. James^d

^a Department of Mechanical, Korea University, Anamdong, 5-Ga, Sungbukgu, 136-713 Seoul, Republic of Korea

^b School of Aeronautics and Astronautics, Purdue University, West Lafayette, IN 47907, USA

^c ADD, 3-Hyun-3, 111 Sunam-Dong, Yuseong-Gu, Taejeon 305-152, Republic of Korea

^d Thermal/Fluid Science & Engineering, Sandia National Lab, P.O. Box 969, Livermore, CA 94551, USA

ARTICLE INFO

Article history:

Received 16 October 2009

Received in revised form 22 August 2010

Accepted 27 August 2010

Available online 18 September 2010

Keywords:

BEM

Two-phase flow

Drop impact

Air entrapment

Aerodynamics effect

Kelvin–Helmholtz instability

Splashing

ABSTRACT

A two-phase flow model using the boundary element method was applied to investigate the physics of a liquid drop impacting onto a solid, dry plate. Xu et al. showed that air pressure plays an important role in splashing: as air pressure was reduced, splashing of an ethanol drop with a Weber number of 838 was suppressed. This remarkable observation provided the motivation for the current modeling effort. We numerically investigate how air pressure affects the behavior of an impacting drop. Surveying both inside and outside the impacting drop, velocities of both the liquid and gas are computed. Simulations show that gas speed, as it is displaced by the falling drop, is more than three times higher than the incoming drop speed. Air entrainment induced by the displaced gas seems to be an important contributor to corona formation, which always precedes any instability, fingering, or splashing of the liquid. To describe drop-impact phenomena, the maximum spreading diameter of the drop and the topology of the impacting fluid are reported as functions of Weber number and gas density.

© 2010 Elsevier Ltd. All rights reserved.

1. Introduction

Drop-impact phenomena are ubiquitous; they are observed in raindrops and in numerous industrial applications such as aerosol deposition, inkjet printing, painting, impact within the cylinders of internal combustion engines, and fire suppression sprays. As shown in classical experiments (Worthington, 1876, 1877, 1908), a drop will spread over the impacting substrate when its surface tension energy is less than its dissipative energy (Aziz and Chandra, 2000). Upon impact, a drop spreads radially and forms a toroidal ring when the ratio of Weber to Reynolds (i.e., We to Re) numbers is fairly low. At intermediate We/Re , an azimuthal instability develops and forms “fingers” at the rim of the spreading ring. If We/Re is further increased, the drop splashes as the fingers disperse into individual droplets. It has been *traditionally* believed that surface tension, viscosity, and substrate roughness (i.e., We , Re , and Ra) are the primary parameters that control drop-impact phenomena (Rein and Delplanque, 2008). In this paper, we investigate splashing mechanisms using the two-phase flow boundary element method (BEM) to account for the somewhat *non-traditional* effects of gas pressure (Xu et al., 2005) at moderate impact speeds and when capillary effects are dominant over viscous effects. The BEM is appropriate for modeling capillary-force-domi-

nant drop-impact phenomena because it accurately replicates the transient topology of an impacting drop.

Pioneering BEM work for drop impact studies was conducted by Oguz and Prosperetti (1990) and Yarin and Weiss (1995) and Weiss and Yarin (1999) with subsequent relevant work by Davidson (2000, 2002), Reznik and Yarin (2002), and Park et al. (2008). In most modeling efforts, the drop is initially assumed to be in contact with the impacting substrate or liquid-film and, therefore, any effects of the air displaced before impact are neglected. Other models do not consider the gas phase at all in their analyses (Bussmann et al., 2000, 1999). Because the surrounding gas was not simulated in these models, this fundamental contributor to splashing could not be addressed. Recent experimental observations confirm that displaced air is instrumental in inducing splashing (Park et al., 2008; Xu et al., 2005). Yoon et al. (2009a, 2007, 2009b) and Liu et al. (2010) showed that finger formation along the toroidal ring of an impacting drop is much better described by the velocity-gradient-dependent Kelvin–Helmholtz (KH) theory than by the density-dependent Rayleigh–Taylor theory (Aziz and Chandra, 2000). Xu (2007) also suggested that coronal splashing can be accurately described with KH instability theory, which requires interaction between the falling drop and displaced air. Moreover, recent studies (Mandre et al., 2009; Mani et al., 2010) indicate that the gas layer squeezed between the substrate and impacting drop (“air entrapment”) provides a variable-pressure cushion (over which the drop slides) that can lead to instabilities that induce splashing.

* Corresponding author. Tel.: +82 2 3290 3376; fax: +82 2 926 9290.

E-mail address: skyoona@korea.ac.kr (S.S. Yoon).

This air entrapment effect is similar to what is observed during drop-drop binary collisions where drops do not immediately coalesce because of a thin gas layer between them (Qian and Law, 1997). Xu et al. (2005), Mandre et al. (2009) and Mani et al. (2010) have all demonstrated that fingering increases with increasing gas pressure, which reinforces the importance of the aerodynamic effects on drop-impact phenomena. Clearly, models should account for these aerodynamics effects, which are extremely difficult to observe experimentally because the aerodynamic-induced ripples are small and ephemeral. Such experimental difficulty is one of the motivations for this computational work.

There is a wealth of literature on drop impact modeling. Numerous authors have implemented volume-of-fluid (VOF) or Level-Set approaches to model free-surface problems because they solve the full Navier–Stokes equations (Azar et al., 2005; Busmann et al., 1999, 2000; Fukai et al., 1993, 1995; Ge and Fan, 2005; Haller et al., 2002; Josserand et al., 2005; Josserand and Zaleski, 2003; Mehdi-Nejad et al., 2003; Mukherjee and Abraham, 2007; Pasandideh-Fard et al., 1996; Reiber and Frohn, 1999; Renardy et al., 2003; Sikalo et al., 2005; Yokoi et al., 2009). While VOF-based approaches continue to improve with the aid of faster computers, their inherent interpolative nature can introduce inaccuracies in surface curvature estimate (and hence, capillary forces). As an example, a typical VOF calculation of fluid sloshing in a tank (Hung and Lee, 1994) exhibits 1% error in volume conservation, whereas a BEM calculation had 0.01% volume error with a similar grid resolution. Also, in this work, we are interested in KH-type inviscid instability, which may be responsible for the instabilities along the free surface that lead to splashing. We are particularly interested in the instability at the interface between gas and liquid. This surface-tension-driven (or capillary-dominated) instability scenario is modeled with the BEM.

2. Model development

2.1. Two-phase flow modeling

Heister (1997) provides a complete description of a BEM application to two-phase flow. In an inviscid, incompressible, axisymmetric flow, it is presumed that the flow dynamics are governed by Laplace's equation: $\nabla^2 \phi = 0$. The BEM uses an integral representation of this equation to provide the connections among the values on the boundary, the local geometry, and the local velocity normal to the boundary, $q = \partial\phi/\partial n$, as follows:

$$\alpha\phi(\vec{r})_i + \int_{\Gamma} \left[\phi \frac{\partial G}{\partial n} - qG \right] d\Gamma = 0, \quad (1)$$

where $\phi(r_i)$ is the local potential, Γ is the boundary of the domain, α is the singular contribution when the integral path passes over the “base point,” and G is the free-space Green's function corresponding to the Laplace equation. For an axisymmetric domain, the free-space Green's function can be expressed in terms of elliptic integrals of the first and second kinds and is a function solely of the instantaneous surface geometry. For this reason, a discrete representation of Eq. (1) can be cast as a linear system of equations relating local ϕ and q values. With discretization, both ϕ and q are assumed to vary linearly between nodes. Because the resulting integrals do not have exact solutions, four-point Gaussian quadrature is used to preserve the second-order accuracy overall.

While this governing equation is linear, it accounts for the nonlinearities of free-surface problems through the boundary condition at the interface. The unsteady Bernoulli equation provides a connection between the local velocity potential and the surface shape at all times. Prior formulations (Heister, 1997; Spangler et al., 1995) have provided a derivation of this connection, which

is suitable for implementation in a Lagrangian surface tracking environment. The dimensionless form of the unsteady Bernoulli equation for a liquid surface is characterized with parameters for the drop radius, a , the impact speed, U , and the liquid density, ρ_l .

$$\frac{\partial\phi}{\partial t} + \frac{1}{2}|\nabla\phi|^2 + P_g + \frac{\kappa}{We} - \frac{Bo}{We}z = 0, \quad (2)$$

where κ is the local surface curvature, P_g is the gas pressure, t is time, and z is the axial direction. The Weber and Bond numbers are defined as $We = \rho_l U^2 a / \sigma$ and $Bo = \rho_l g a^2 / \sigma$, respectively, where σ and g are the liquid surface tension and gravitational acceleration, respectively.

Using the Eulerian–Lagrangian transformation for the surface nodes moving at the velocity of the liquid, the dimensionless Bernoulli equation for the free surface of the liquid becomes:

$$\frac{D\phi}{Dt} = \frac{1}{2}|\nabla\phi|^2 - P_g - \frac{\kappa}{We} + \frac{Bo}{We}z. \quad (3)$$

where D/Dt denotes the material or Lagrangian derivative. Physically, this Bernoulli equation is in a Lagrangian form that is suitable for application to fluid elements moving at the local velocity of the free surface. Eq. (3) includes the effects of dynamic pressure, local gas-phase pressure, capillary pressure, and hydrostatic pressure, respectively.

An analogous treatment for the gas phase yields:

$$\varepsilon \frac{D\phi_g}{Dt} = \varepsilon \nabla\phi \cdot \nabla\phi_g - \frac{\varepsilon}{2}|\nabla\phi_g|^2 - P_g, \quad (4)$$

where ε is the gas/liquid density ratio ($\varepsilon = \rho_g/\rho_l$). These ordinary differential equations are integrated in time using a fourth-order Runge–Kutta scheme to solve for the velocity potential and to predict the motion of the free surface. Highly distorted surface have points on the free surface that tend to bunch in regions of higher curvature as a result of the free-surface motion. To improve the resolution of highly distorted surfaces, the points on the free surface are redistributed at each time step using a cubic spline fit to the instantaneous shape. Fourth-order accuracy is also employed in computing all surface derivatives to maximize the accuracy of the surface evolution method. The Laplace equation is solved to update velocities and this process is repeated for a set period.

It is difficult to calculate contact angles for inviscid flows (Davidson, 2000). However, the contact angle is specified to correspond to a real contact angle. BEM nodes in contact with a substrate wall are given a “no penetration” boundary condition; i.e., their normal velocity components are zero, $q = \partial\phi/\partial n = 0$. When this boundary condition is enforced, it establishes a relatively large value for the advancing contact angle (in excess of 90°). Davidson (2000) recommends fixing the value at 90° while also specifying that parametric fourth derivatives of r and z on the boundary be zero at the contact line. These criteria yield results similar to observed experimental trends for drop spreading. In other models, the advancing contact angle has been modeled as a function of the capillary number, $Ca = We/Re$; see the works of Blake and Haynes (1969), Hoffman (1975), Jiang et al. (1979), Seebergh and Berg (1992), Schneemilch et al. (1998), Ranabothu et al. (2005). The capillary number has been related to the splashing criteria (Cossali et al., 1997; Mundo et al., 1995; Rein and Delplanque, 2008; Yarin and Weiss, 1995), which is also dependent upon the substrate roughness (Xu, 2007). Clearly, depending upon the technique, the contact angle can be a strong function of surface tension, viscosity, and substrate roughness. In the validation section that compares our inviscid result to the full Navier–Stokes solution of Fukai et al. (1993), we demonstrate that the inviscid assumption does not significantly change the topology of impacting drops on a smooth surface in the capillary-dominated regime we have considered in this effort.

2.2. Interior velocity computation

Gas velocities, $\partial\phi_i/\partial z$ and $\partial\phi_i/\partial r$, at any point within the computational domain, are computed as derivatives in the velocity potential of the Laplace equation, (1), with $\alpha = 2\pi$ for point r_i on a smooth surface (or boundary) and $\alpha = 4\pi$ for an interior fluid point (Sato et al., 1994; Wang et al., 1996, 2005). When solving for ϕ at an interior node, the integral over the boundary does not include any nodes on the interior. Because of this, singularities that arise in the elliptic integral for the boundary nodes do not occur because the segment will never contain a base point, "i". To calculate ϕ at an interior node, Eq. (1) can be rearranged as:

$$\phi_i = \frac{1}{4\pi} \int_{\Gamma} \left[\phi \frac{\partial G}{\partial n} - qG \right] d\Gamma. \quad (5)$$

Following the same discretization procedure used for nodes on the boundary, Eq. (1) becomes:

$$2\pi\phi_i = D_{ij}\phi_j - S_{ij}q_j, \quad (6)$$

where subscript i denotes an interior node and subscript j denotes a node on the boundary, and D and S represent the kernels for the source and doublet integrals, respectively (Hilbing, 1996). When solving for an individual interior node, D and S become row vectors and thus the value of ϕ_i is given by this single equation. D and S must already be known before ϕ_i can be calculated from Eq. (6). Therefore, the Laplace equation must be solved for the nodes on the boundary before it is solved for interior nodes.

The free-space Green's function solution to the axisymmetric Laplacian is:

$$G = \frac{4rK(p)}{\sqrt{a}}, \quad (7)$$

and from Heister (1997),

$$\frac{\partial G}{\partial n} = \frac{-2}{\sqrt{a}} \left\{ n_r K(p) + \frac{E(p)}{c} [dn_r + 2rn_z(z - zi)] \right\}, \quad (8)$$

where p , a , c , and d are defined as:

$$p = \frac{(r - r_i)^2 + (z - z_i)^2}{(r + r_i)^2 + (z - z_i)^2}, \quad (9)$$

$$a = (r + r_i)^2 + (z - z_i)^2, \quad (10)$$

$$c = (r - r_i)^2 + (z - z_i)^2, \quad (11)$$

$$d = r^2 - r_i^2 - (z - z_i)^2. \quad (12)$$

Differentiating Eq. (5) with respect to the base point at "i" yields

$$\frac{\partial\phi_i}{\partial z} = \frac{1}{4\pi} \int_{\Gamma} \left[q \frac{\partial G}{\partial z_i} - \phi \frac{\partial^2 G}{\partial n \partial z_i} \right] d\Gamma, \quad (13)$$

$$\frac{\partial\phi_i}{\partial r} = \frac{1}{4\pi} \int_{\Gamma} \left[q \frac{\partial G}{\partial r_i} - \phi \frac{\partial^2 G}{\partial n \partial r_i} \right] d\Gamma. \quad (14)$$

The values of $\partial\phi_i/\partial z$ and $\partial\phi_i/\partial r$ are determined after values of both ϕ and q have been calculated for every node on the boundary using the BEM solution to the Laplace equation. Because ϕ and q are already known, the D and S matrices are completely determined from ϕ and q for the nodes on the boundary and do not need to be integrated in time. Interior node calculations only have to be performed at times when data about the interior nodes are desired. Alternate forms of the derivatives of ϕ are also available (Oguz and Prosperetti, 1990, Eqs. (A1) and (A2)). Derivation of the Green's function is available in Appendix A.

Computing velocities both inside and outside the impacting drop is important because it addresses the momentum exchange between the falling drop and the surrounding gas. Velocities are calculated as the derivative of the velocity potential from the governing Laplace equation in its integral form. Analytic kernels are derived to represent the derivative exactly, with solutions obtained through Gaussian quadrature. The analytic kernels compute the accelerating gas velocities below the falling drop that impart their effects on the drop. Random numbers are uniformly seeded throughout the computational domain to specify where local velocities of liquid and gas phases are calculated and are contoured.

2.3. Computational details

The schematic of the falling drop onto a smooth substrate is presented in Fig. 1. The outer fixed boundary of the gas domain

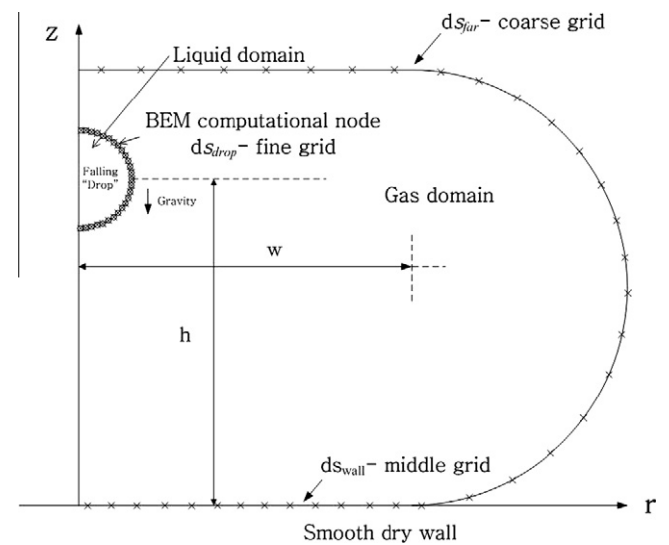


Fig. 1. A schematic of the computational domain. The liquid drop is released at height of h (axially) within the gas domain of width w in the radial direction.

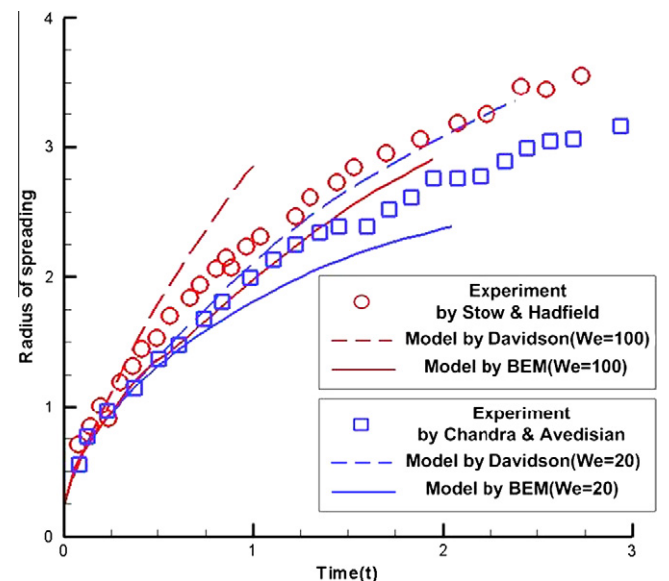


Fig. 2. Spreading radius histories from BEM simulations and experimental data. Comparisons are made at $We = 100$ (red) and $We = 20$ (blue). (For interpretation of the references to color in this figure legend, the reader is referred to the web version of this article.)

is sufficiently large to encompass the liquid drop for the entire duration of the calculation and is placed far enough from the liquid phase to ensure that its influence on the flow field around the drop is negligible. A coarse grid is used along this outer gas boundary. Nodes are implemented at the outer boundary to close the computational domain. The impacting substrate is a smooth, impenetrable, dry plate (i.e., $q = 0$). Dissipative energy induced by the

substrate's roughness is not considered in this inviscid model and, thus, the post-impact energy of the liquid is overestimated, especially if the substrate's roughness is relevant.

Processor time depends on the grid size and the fine grid resolution applied around the liquid drop adds significant computational expense. Sufficiently accurate initial grid spacing for the inner/outer boundary was determined through a grid convergence

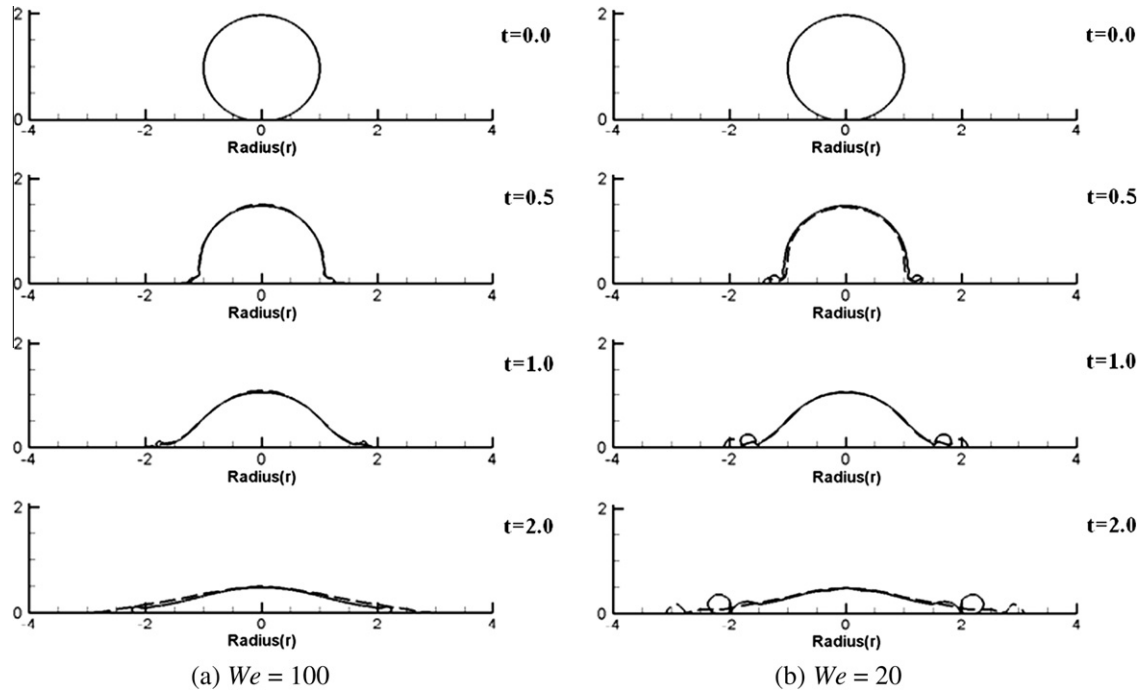


Fig. 3. Time series variation in drop profiles for (a) $We = 100$ and (b) $We = 20$. The solid and dashed curves represent the computational results from the present study and Davidson's (2000), respectively.

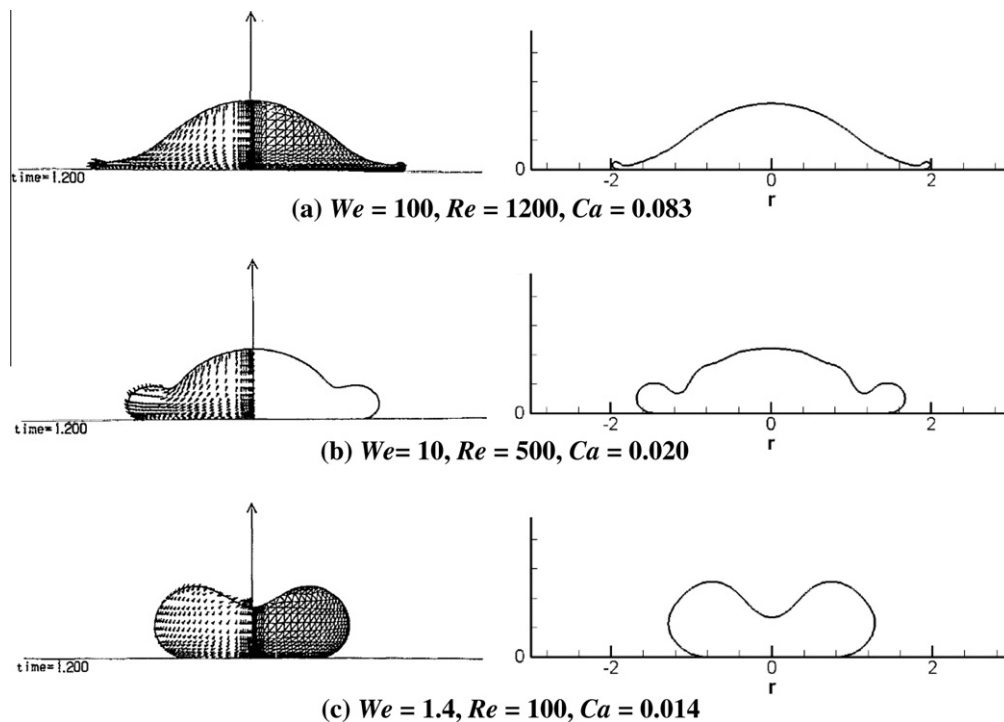


Fig. 4. Comparisons of drop topology between Fukai et al.'s (1993) full Navier–Stokes solution in the left column and our inviscid BEM in the right column. Viscosity effects seem of secondary importance because results differ minimally. Fukai et al.'s (1993) non-dimensional time scale is equivalent to ours. Snapshots are at $t^* = 1.2$ ($Ca = We/Re$).

study (Park et al., 2008); spacing for the liquid surface (ds_{drop}) and for the wall boundary (ds_{wall}) with respect to the drop radius are $ds_{\text{drop}}/a = 0.02$ and $ds_{\text{wall}}/a = 0.04$, respectively. At the start of the computation, there are $\pi/0.02 \approx 157$ nodes implemented along the semi-circle free surface. Grid spacing for the outer boundary (ds_{far}) is $ds_{\text{far}} = 5ds_{\text{wall}}$. A typical unsteady calculation uses 250 nodes along the liquid drop and 400 nodes along the outer boundary because, upon impact, the topology of the drop changes, resulting in longer free surface lengths (requiring more closely spaced nodes before impact).

The drop center starts $4a$ above the impact surface. The drop's dimensionless radius is unity (e.g., the reference length is the drop's radius, a) and the drop's bottom is situated at $z/a = 3$. Thus, there are $\Delta t^* = \Delta t U/a = 3$ dimensionless time units before impact. The drop is assigned initial speed U_i and velocity gained through conversion of potential energy is ignored yielding a final impact speed of $U_f = \sqrt{U_i^2 + 2gh} \approx U_i$; the magnitude of the $2gh$ term comprises less than 0.1% of the total speed, U_f , for the experiments of Xu et al. (2005).

Numerical simulations confirmed that the $h = 4a$ starting condition was sufficiently far from the wall to allow proper calculation of the pressure increase below the falling drop before impact. It should be noted that at higher We , using a sufficient number of computational nodes near the impact region is necessary to capture the detailed physics of splashing.

3. Results and discussion

3.1. Comparison to Davidson's and Fukai's models

Figure 2 compares the histories of the spreading liquid radius to both data and the models of several authors for $We = 100$ and $We = 20$, respectively. The solid and dashed curves represent the BEM predictions from our model and Davidson's (2000), respectively. The experimental data of Stow and Hadfield (1981) and Chandra and Avedisian (1991) are provided for comparison. Upon reducing We from 100 to 20, slower spreading is evident because of the increased relative influence of surface tension, which tends to constrain the fluid. It is notable that Davidson's result, based on an inviscid model, *over-predicts* the spreading rate, especially for $We = 100$ where surface tension is a smaller fraction of the total force. Though similar spreading for $We = 100$ was observed using our inviscid model, our result slightly *under-predicts* the spreading rate because of addition of artificial viscosity by diffusive numerical filters (Yoon and Heister, 2004). Notwithstanding these observations, the Ohnesorge number is small $Oh = We^{1/2}/Re \approx 10^{-3}$ for these cases and here viscous forces are unlikely to play a major role. Overall, the differences are small and within the suite of experimental and modeling uncertainties.

Figure 3 compares our BEM drop profiles (solid curve) to those of Davidson (dashed curve) for $We = 100$ and 20. Results agree for

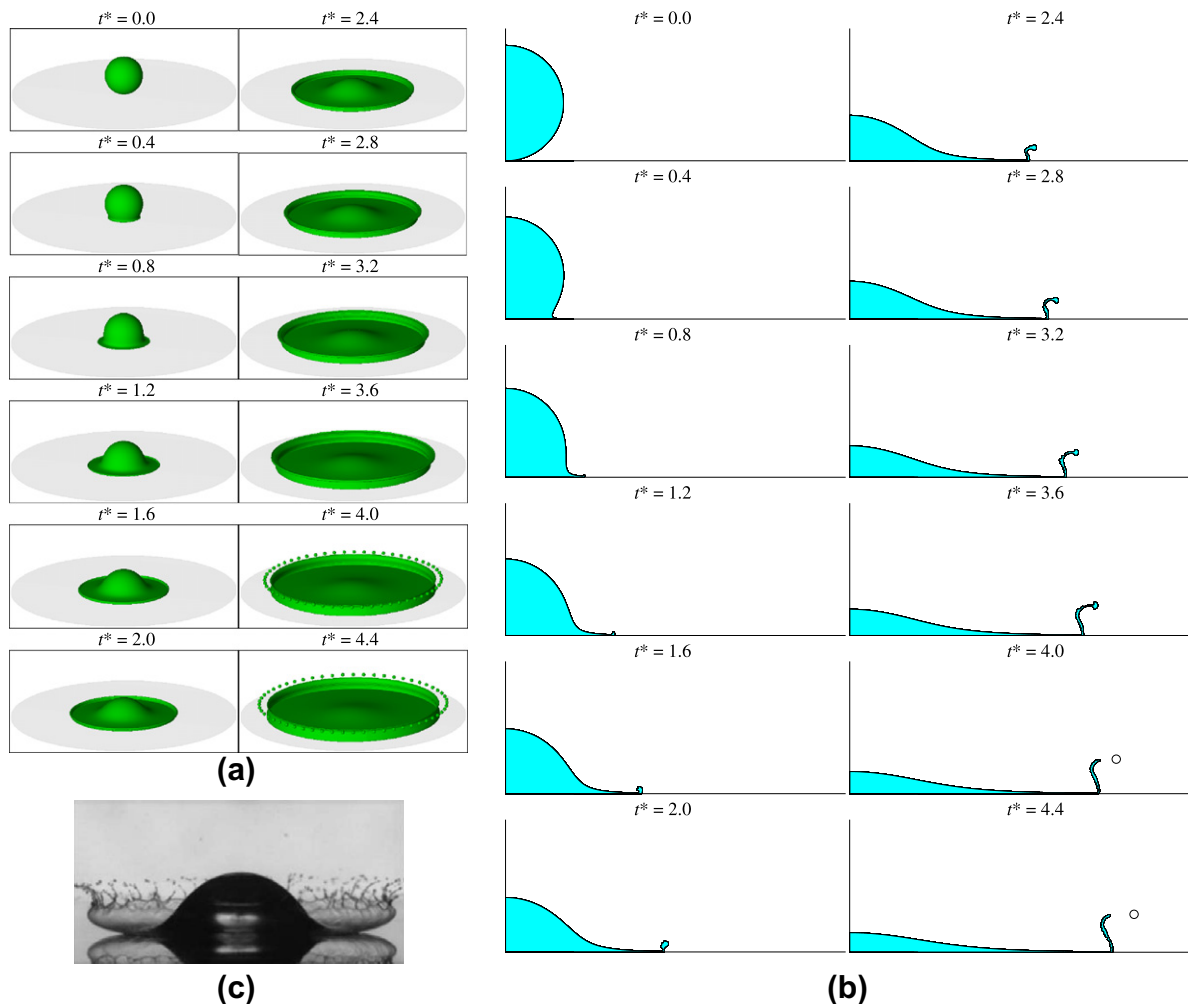


Fig. 5. (a) Formation of the rising corona and the resulting splashed droplets, whose population is predicted through Ponstein's (1959) linear vortex ring instability theory. (b) Side-view snapshots of (a). (c) Snapshot of a splash from the Xu et al. (2005) experiment at $t^* = 1.2$.

the larger Weber number, while notable differences are evident at the lower Weber number. Differences are attributed to the numerical filter (see Yoon and Heister (2004) for further details) that adds artificial viscosity to our simulations. It is evident that the size of the corona (toroidal ring due to mass accumulation in the region) grows as the relative influence of the surface tension increases (smaller We); rim formation is related to surface tension. Previous authors (Fukai et al., 1993; Stow and Hadfield, 1981; Worthington, 1876) also observed these rims and their growth with time. While the experimental and numerical works of these authors consider viscosity, the rim still appears in Davidson's and our inviscid simulations. However, the addition of diffusion (viscosity) through a

numerical filter can expedite the appearance of the rim; our BEM simulation captures the rim at $We = 100$ and demonstrates better agreement with the experiments (Stow and Hadfield, 1981) than the results of Davidson. These simulations suggest that rim appearance is at least partly due to surface tension and its appearance is enhanced by viscosity (manifested through the addition of numerical diffusion in our model).

Figure 4 compares our BEM results to the full Navier–Stokes solution of Fukai et al. (1993) for $We = 100, 10$, and 1.4 . Fukai et al. (1993) varied the Reynolds numbers by varying viscosity. They showed that the maximum spreading radius increases (or, the thin-film thickness decreases) with larger Re and We , and vice

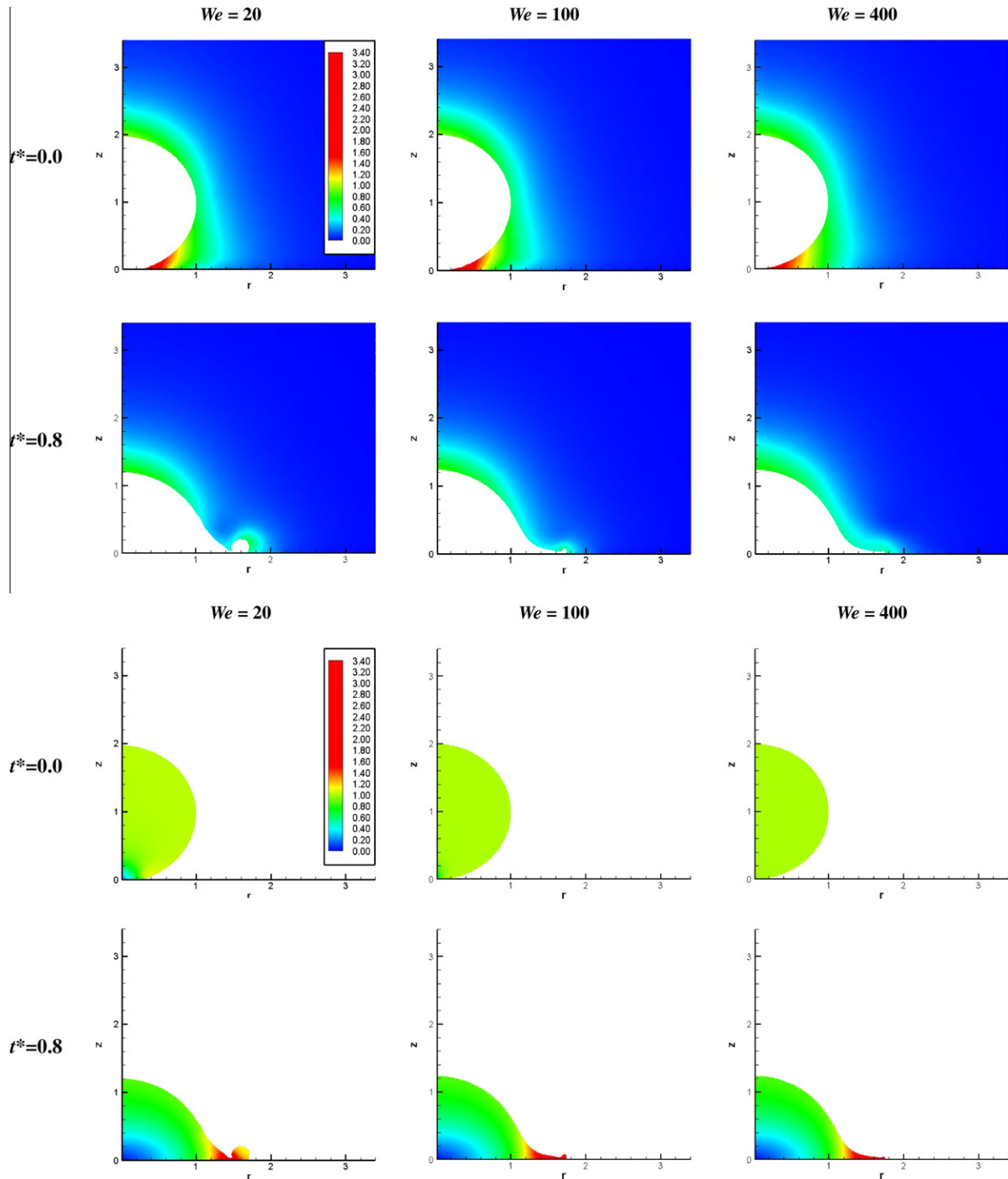


Fig. 6. Time series variations of velocities for both liquid and gas phases at various We .

versa. Inclusion of viscosity yields a velocity profile in the vertical direction because the velocity close to the wall approaches zero due to the no-slip boundary condition. Our BEM model is inviscid and, thus, the no-slip boundary condition cannot be enforced. However, we impose a no-penetration boundary condition at the solid surface; i.e., the normal velocity component is set equal to zero, $q = \partial\phi/\partial n = 0$. This boundary condition is different from Davidson's (2000) where $u = \partial\phi/\partial z = 0$. Nevertheless, because these conceptual model differences do not yield significant qualitative differences, the velocity profile does not seem to be a critical factor in splashing, especially at high We or Re numbers. Because our inviscid model cannot develop a velocity profile within the spreading ring but splashing is still simulated, it means that an accurate velocity profile is not necessary to simulate spreading and splashing of an impacting drop. By comparing our results to those of Fukai et al. (1993), it again suggests that viscosity is not a primary factor controlling splashing (at least for the range of parameters considered here).

The capillary wave of maximum amplification has wavelength $\lambda = \sigma/(\rho_l U^2)$, according to Renardy et al. (2003), but waves appear only when $\lambda < a$ or $We > 1$. A rough estimate for a 1-mm-radius water drop yields $\lambda = 0.7$ mm for $We = 1.4$ as shown in Fig. 4c at $t^* = 1.2$. An earlier image ($t^* = 0.4$) has wavelength of 0.6–0.7 mm, consistent with the prediction of Renardy et al. (2003). It is worth noting that to observe multiple waves (staircase or pyramidal structures) on the drop surface, $WeCa$, or We^2/Re , must be less than 1, which is the case for Fig. 4b and c.

3.2. Prediction of the number of splashed droplets

The BEM was used to simulate the experiment of Xu et al. (2005). Therein, the radius of the incoming alcohol drop was $a = 1.7$ mm with impact velocity $U_f = 3.74$ m/s. Alcohol density

and surface tension were $\rho_l = 789$ kg/m³ and $\sigma = 0.0224$ kg/s², respectively, yielding $We = \rho_l U^2 a / \sigma = 837.9$. The density ratio was $\varepsilon = \rho_g / \rho_l = 0.00158$. The dimensionless surrounding gas pressure, $P_g^* = P_g / U^2 \rho_l$, was $P_g^* = 9.18$ when $P_g = 101.325$ kPa.

Figure 5a shows time-series snapshots of the simulated splashing event corresponding to Xu et al.'s (2005) experiment using visualization software Tecplot. The instant of impact is $t^* = 0.0$ and the simulation was initiated at $t^* = -3.0$. It took about $t^* = 4.0$ (equivalent to real time, $t = t^* a / U = 1.82$ ms) for the rising corona to elongate and finally break into "droplets" ("drop" refers to the impacting drop). Equivalent side-view snapshots are shown in Fig. 5b. Experimentally, splashed satellite droplets form notably earlier than $t = 1.82$ ms (time of snapshot shown in Fig. 5c is 0.552 ms, $t^* = 1.2$). In fact, droplets are evident in Fig. 5c even as the upper half of the drop is still collapsing toward the substrate. One of the reasons for this discrepancy between the BEM prediction and the experiment is that the vortex-ring model of Ponstein (1959) can only be applied after complete detachment of the ring from the liquid due to limitations imposed by the axisymmetric simulation (i.e., splashed droplets are not formed until the vortex ring is completely separated from the main drop and no nonlinearities are included in the model). Experimental splashes show fingering throughout the rising corona before its complete detachment and the corona does not form a "ring," rather, a number of "fingers." To partially reconcile this discrepancy between the simulation and experiment, we presume that as soon as a ring is formed at the periphery of the spreading drop (i.e., the distance between the closest nodes in the necking ring region is $< 10\%$ of the node's initial spacing), the ring is assumed detached from the bulk fluid, immediately breaking up into splashed droplets. Despite this timing discrepancy, our use of Ponstein's linear theory predicts 56 splashed droplets while the corresponding experiment had 52 ± 2 splashed droplets at the rim of the corona.

Although the splashing event of Xu et al.'s experiment at $We = 838$ was successfully replicated in this study, numerical instability becomes an issue at larger We . Capturing many small

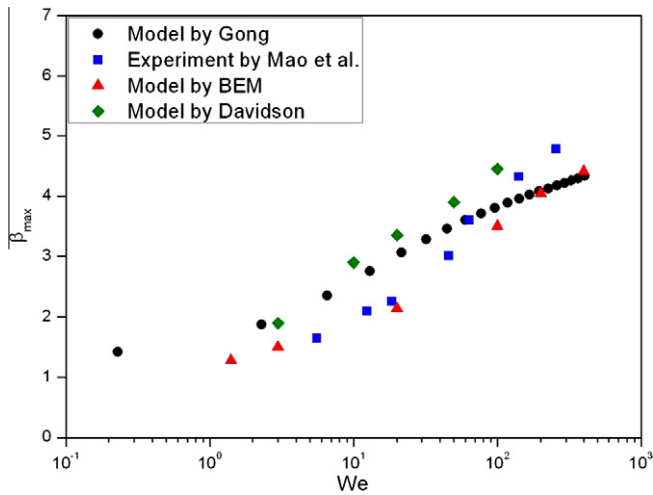


Fig. 7. The Weber number effect on the dimensionless maximum diameter (i.e., $\beta_{\max} = D_{\max}/D$). Comparisons are drawn between the data from an analytical model (Gong, 2005), numerical results (BEM simulations by Davidson (2002) and us), and experiments (Mao et al., 1997).

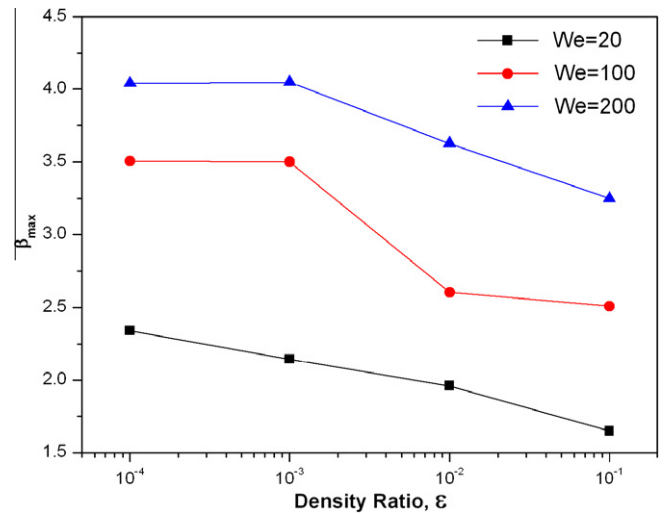


Fig. 8. Effect of ε on $\beta_{\max} = D_{\max}/D$ for $We = 20, 100,$ and 200 .

Table 1
Parameter variation as a function of density ratio, $\varepsilon = \rho_g/\rho_l$.

$We = \rho_l U^2 a / \sigma$	20				100				200			
$\varepsilon = \rho_g / \rho_l$	10^{-4}	10^{-3}	10^{-2}	10^{-1}	10^{-4}	10^{-3}	10^{-2}	10^{-1}	10^{-4}	10^{-3}	10^{-2}	10^{-1}
$P_g^* = P_g / \rho_l U^2$	6.9	69	690	6900	1.38	13.8	138	1380	0.69	6.9	69	690
P_g [kPa]	10.13	101.3	1013	10,130	10.13	101.3	1013	10,130	10.13	101.3	1013	10,130

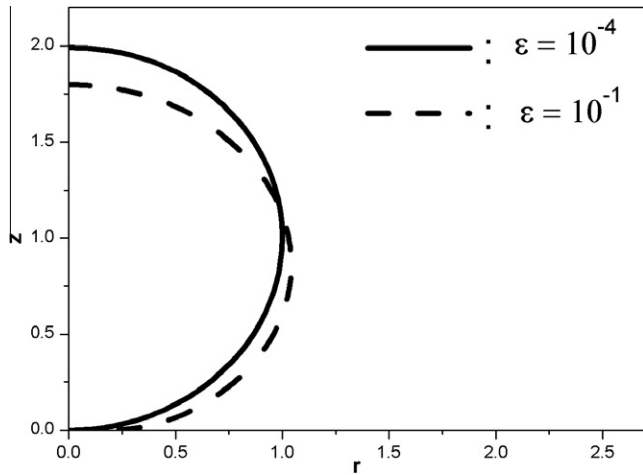


Fig. 9. Effect of ϵ on drop shape upon impact at $We = 200$.

droplets at high We is computationally challenging because nodes tend to form a zig-zag pattern at the free surface of the rising ring and an intractable number of nodes is required to fully resolve these higher We scenarios.

3.3. Variation as a function of Weber number

The effects of Weber number on drop velocities are considered in Fig. 6, which shows the speed of the gas (top two rows) and liquid (bottom two rows) when $t^* = 0.0$ and 0.8 for $We = 20, 100,$ and 400 . Gas displaced from under the falling drop before impact achieves speeds of 3–4 times the drop speed (e.g., $|(u^2 + v^2)^{1/2}|_{\max}/U$) through momentum exchange between the falling drop and the initially stagnant gas. The gas speed around the drop, except in the displaced region, is approximately equal to the impact speed (i.e., see the green color level). At $t^* = 0.8$, the drop periphery has a high velocity while the drop center is nearly stagnant (blue) against the unyielding wall; this trend is consistent with observations of Fukai et al. (1993) and Trapaga and Szekely (1991).

At lower We , a toroidal ring forms because surface tension decelerates the spreading front. While drop topology changes as a function of We , its variation does not seem to have a significant effect on the general distribution of the interior velocities.

Figure 7 shows the non-dimensional maximum diameter of the impacting drop for a range of We , where β_{\max} is the ratio of the maximum drop diameter to the initial drop diameter $\beta_{\max} = D_{\max}/D$ or a_{\max}/a . Our BEM simulations are compared to those of Gong (2005) and Davidson (2002) and the experimental data of Mao et al. (1997). Gong’s model considers the effect of boundary layer

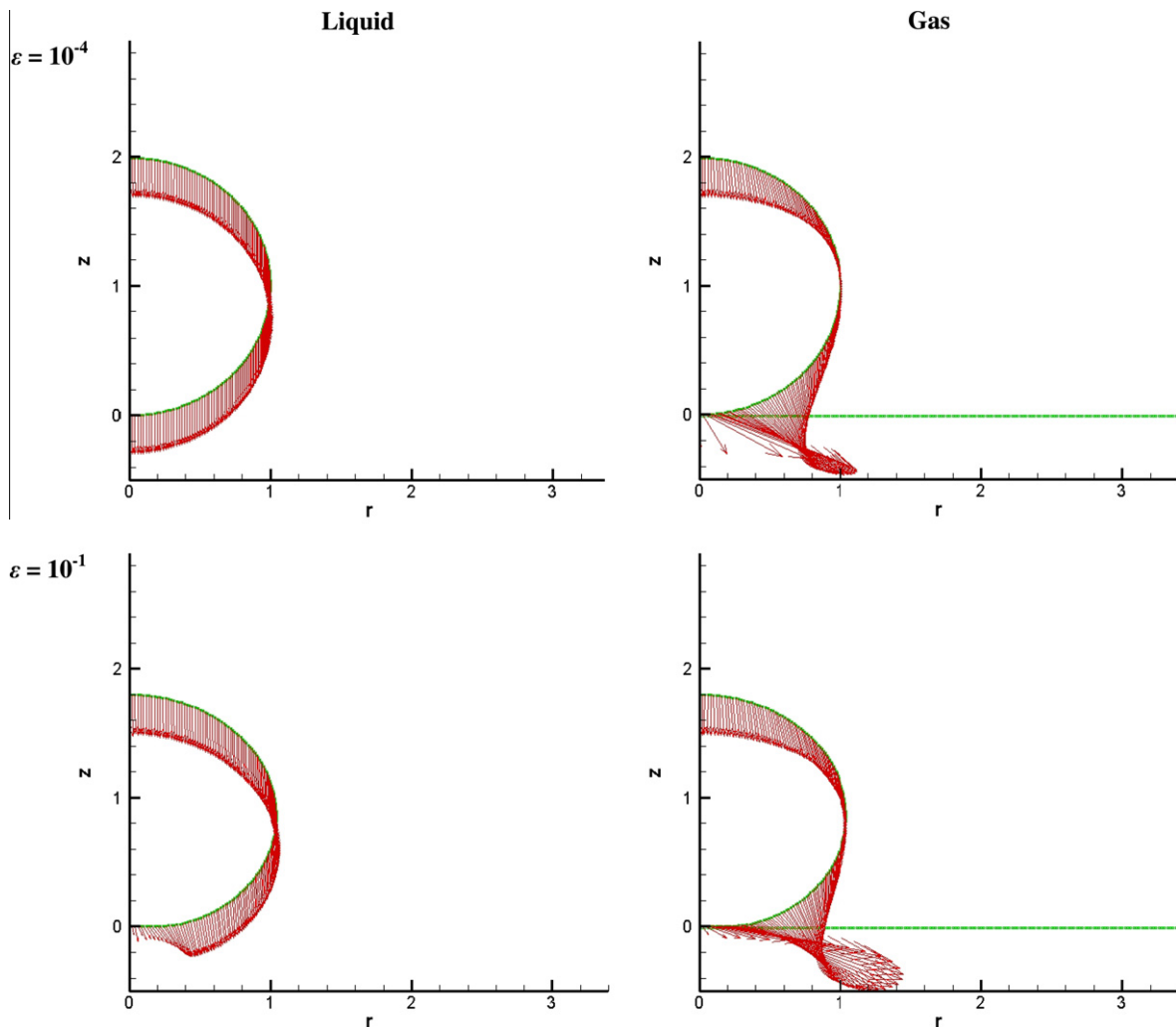


Fig. 10. The density ratio effect on interface velocities of liquid (left column) and gas (right column) upon impact. The red arrows indicate velocity vectors and the green dots represent the interface between liquid and gas. Here, $We = 200$. (For interpretation of the references to color in this figure legend, the reader is referred to the web version of this article.)

thickness and assumes “hockey puck” deformation of the drop upon impact as:

$$6 \frac{We}{\sqrt{Re}} \beta_{\max}^4 + 30(1 - \cos \theta_a) \beta_{\max}^2 + \frac{80}{\beta_{\max}} = 20We + 120, \quad (15)$$

where θ_a is the advancing angle of 97° based on the measurement of Bussmann et al. (1999). The preceding equation is solved using Newton’s method subject to given Weber and Reynolds numbers. As shown in Fig. 7, our BEM results slightly under-predict the spreading diameter while Davidson (2000) tends to over-predict. In general, the numerical predictions are in quantitative agreement with the experimental data, especially at low Weber numbers, $We < 20$.

3.4. Variations as a function of gas density

The effect of gas pressure (or density because it is assumed that the gas obeys the Ideal Gas Law) is studied by varying the density ratio, $\varepsilon = \rho_g/\rho_l$, from 10^{-4} to 10^{-1} . The details of the parametric variation for the gas density study are summarized in Table 1; ρ_g is increased to increase ε and σ is decreased to increase We .

Figure 8 shows the dimensionless maximum diameters of the impacting drops, β_{\max} , for $We = 20, 100,$ and 200 , as ε increases. In each case, as the gas density increases, the maximum spreading

distance decreases; evidence that the exchange of momentum with increasingly dense gas limits liquid spread.

Figure 9 shows the effect of gas pressure on drop deformation at $We = 200$. The drop deforms into an oblate spheroid just prior to impact at elevated gas pressures. When $We = 200$, it takes a substantially large gas pressure (i.e., 100 atm) to deform the drop before impact. When the Weber number is higher ($We = 838$), it takes only a few atmospheres (e.g., 0.5–2.0 atm) to deform the drop (Park et al., 2008). Thus, a liquid with relatively high surface tension maintains a spherical shape even at fairly high gas pressures while a liquid with relatively low surface tension more easily deforms into an oblate spheroid before impact.

Figure 10 shows the variation in velocity vectors along the drop surface at the instant of impact for various density ratios, $\varepsilon = 10^{-4}$ and 10^{-1} . The figures in the left and right columns are the vectors for liquid and gas, respectively. The gas speeds show more variation than the liquid speeds because of conservation of momentum. As the gas is displaced from below the drop, it is imbued with radial momentum, but its radial momentum component decreases as the density ratios increases from $\varepsilon = 10^{-4}$ to 10^{-1} . Also, when $\varepsilon = 10^{-1}$, the liquid velocity near the contact region is notably reduced by the increased inertia of the dense gas (see the bottom figure in the left column in Fig. 10).

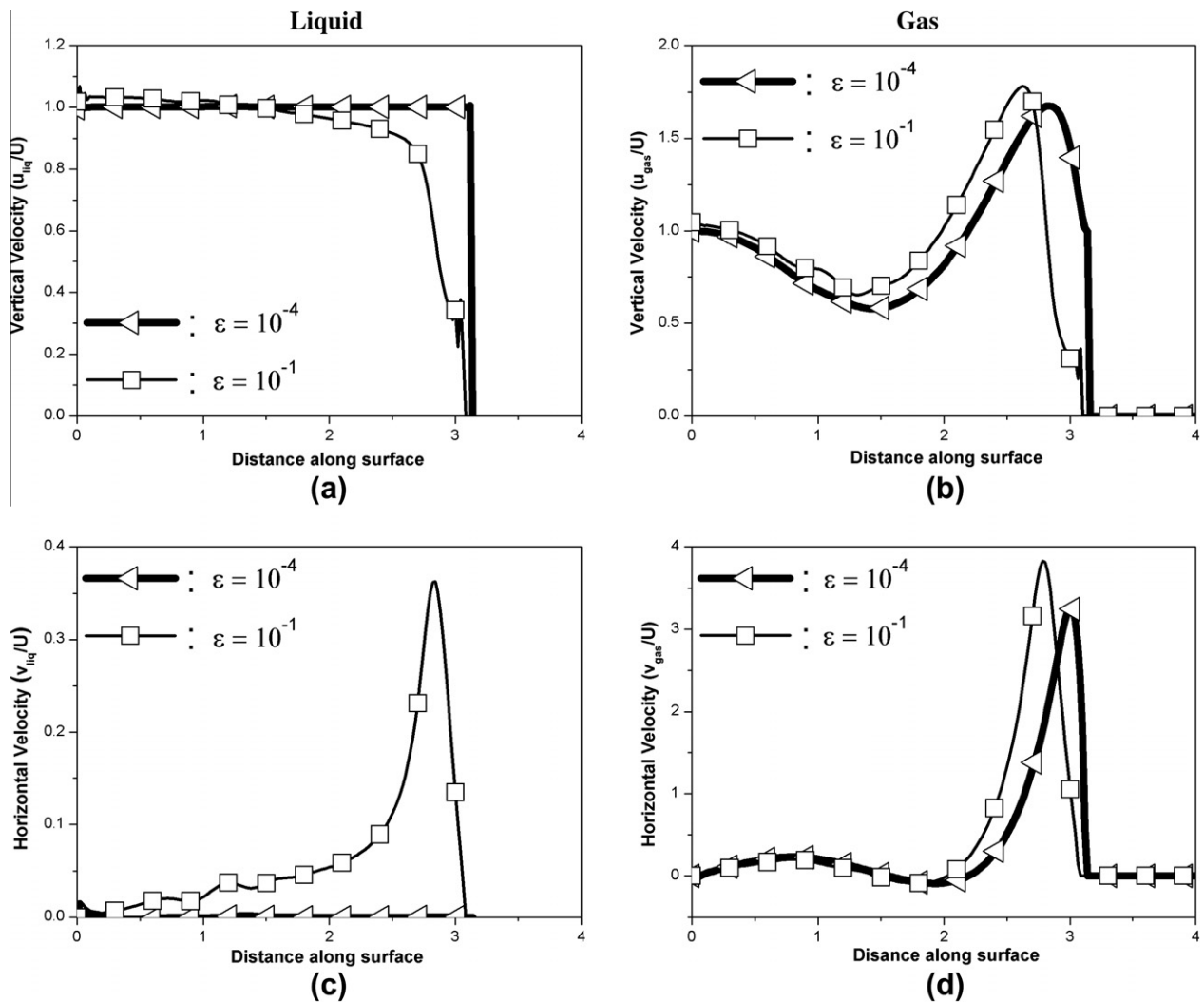


Fig. 11. Interface velocities of the liquid and gas at various density ratios upon impact. These quantitative data are in conjunction with the qualitative data shown in Fig. 10; (a) vertical liquid velocity, (b) horizontal liquid velocity, (c) vertical gas velocity, and (d) horizontal gas velocity. The distance range on the x-axis represents the location of the drop surface, starting from the top (0) to the impact point at the liquid bottom (π). Here, $We = 200$.

Figure 11 is a quantitative comparison of the velocity vectors shown in Fig. 10. The left and right columns are the velocities for liquid and gas, respectively. The first and second rows indicate the vertical (z -direction) and horizontal (r -direction) velocities, respectively. Zero and π on the x -axis indicate the drop's top and bottom, respectively. Increasing the gas pressure has a prominent effect on surface velocities of the liquid and even more so for the gas; the BEM nodes near the impact region (i.e., π on the x -axis) show large velocity changes. Clearly, the magnitudes of velocity variations for the gas are much larger than those for the liquid. Toward the drop's bottom, velocities increase in both the z and r -directions, but the velocities quickly go to zero at the bottom center, π , upon impact. For the liquid, the drop retains nearly zero horizontal velocity along most of the surface when $\varepsilon = 10^{-4}$, although the horizontal velocity is notably affected when the density ratio reaches $\varepsilon = 10^{-1}$; see Fig. 11b.

4. Conclusion

The BEM was applied to compute fluid velocities that reflect the momentum exchange between a falling drop and the surrounding gas. This BEM model both assesses the characteristics (velocities) of both liquid and gas phases before and throughout impact, and estimates air displacement velocities due to the falling drop. To validate our model, it was compared to both experimental and numerical data (Chandra and Avedisian, 1991; Davidson, 2000; Fukai et al., 1993; Stow and Hadfield, 1981) showing both quantitative and qualitative agreement. Upon increasing We , the drop spreads more rapidly and widely; the rim size at the periphery of the spreading liquid was also reduced because of decreased surface tension forces. The spreading diameter decreased as the density ratio (ρ_g/ρ_l) or air pressure increased, indicating that the exchange of momentum with the gas limited liquid spreading. Our computations show that the air velocity exceeds the impact speed of the drop by more than a factor of 3. Displaced air may contain sufficient momentum to cause ripples along the drop surface, and then KH-type inviscid instability may take place. The BEM results are valid under the assumption that both liquid and gas are inviscid and incompressible and that the entire event falls into the capillary-dominant regime. In high-speed impact regimes, viscosity and compressibility may be important. Also, boundary layer development during viscous spreading may enhance finger formation at the periphery.

Acknowledgments

This research was supported by Research Center of Breakthrough Technology Program through the Korea Institute of Energy Technology Evaluation and Planning (KETEP) funded by the Ministry of Knowledge Economy (2009-3021010030-11-1). This study was partly supported by a grant from the cooperative R&D Program (B551179-08-03-00) funded by the Korea Research Council Industrial Science and Technology, Republic of Korea. The last author acknowledges that Sandia is a multiprogram laboratory operated by Sandia Corporation, a Lockheed Martin Company, for the United States Department of Energy's National Nuclear Security Administration under Contract DE-AC04-94AL85000.

Appendix A

$$\frac{\partial^2 G}{\partial n \partial z_i} = \frac{-2(z-z_i)}{a^{3/2}} A - \frac{2}{\sqrt{a}} (B + C + H), \quad (\text{A1})$$

$$\frac{\partial G}{\partial z_i} = \frac{16r^2 r_i (z-z_i)}{\sqrt{a^5}} F_1(p) + \frac{4r(z-z_i)K(p)}{\sqrt{a^3}}, \quad (\text{A2})$$

$$\frac{\partial^2 G}{\partial n \partial r_i} = \frac{2(r+r_i)}{\sqrt{a^3}} L - \frac{2}{\sqrt{a}} (M + NO + P), \quad (\text{A3})$$

$$\frac{\partial G}{\partial r_i} = \frac{-8r[rr_i^2 - r^3 - r(z-z_i)^2]}{\sqrt{a^5}} F_1(p) - \frac{4(r+r_i)rK(p)}{\sqrt{a^3}}, \quad (\text{A4})$$

and

$$A = K(p)n_r + \frac{E(p)}{c} [dn_r + 2r(z-z_i)n_z], \quad (\text{A5})$$

$$B = \frac{4n_r(z-z_i)rr_i}{a^2} F_1(p), \quad (\text{A6})$$

$$C = \left[\frac{-4(z-z_i)rr_i}{ca^2} F_2(p) + \frac{2(z-z_i)E(p)}{c^2} \right] [dn_r + 2r(z-z_i)n_z], \quad (\text{A7})$$

$$H = \frac{E(p)}{c} [2(z-z_i)n_r - 2rn_z], \quad (\text{A8})$$

$$L = K(p)n_r + \frac{E(p)}{c} [dn_r + 2r(z-z_i)n_z], \quad (\text{A9})$$

$$M = \frac{-2n_r[rr_i^2 - r^3 - r(z-z_i)^2]}{a^2} F_1(p), \quad (\text{A10})$$

$$N = \frac{2[rr_i^2 - r^3 - r(z-z_i)^2]}{ca^2} F_2(p) + \frac{2(r-r_i)E(p)}{c^2}, \quad (\text{A11})$$

$$O = dn_r + 2r(z-z_i)n_z, \quad (\text{A12})$$

$$P = \frac{2E(p)n_r r_i}{c}. \quad (\text{A13})$$

$F_1(p)$ and $F_2(p)$ are integrals that result from differentiation of the elliptic integrals in Eq. (6).

$$F_1(p) = \int_0^{2\pi} \frac{\sin^2 \Psi}{\sqrt{[1 - (1-p)\sin^2 \Psi]^3}} d\Psi, \quad (\text{A14})$$

$$F_2(p) = \int_0^{2\pi} \frac{\sin^2 \Psi}{\sqrt{1 - (1-p)\sin^2 \Psi}} d\Psi, \quad (\text{A15})$$

and are related to the elliptic integrals $K(p)$ and $E(p)$ as follows:

$$F_1(p) = \frac{-a^2}{4(z-z_i)rr_i} \frac{\partial E}{\partial z_i} = \frac{a^2}{2[rr_i^2 - r^3 - r(z-z_i)^2]} \frac{\partial E}{\partial r_i}, \quad (\text{A16})$$

$$F_2(p) = \frac{a^2}{4(z-z_i)rr_i} \frac{\partial K}{\partial z_i} = \frac{-a^2}{2[rr_i^2 - r^3 - r(z-z_i)^2]} \frac{\partial K}{\partial r_i}, \quad (\text{A17})$$

The integrals $F_1(p)$ and $F_2(p)$ are calculated numerically using the Gaussian quadrature.

It is important to note that the terms $\partial\phi/\partial z_i$, $\partial q/\partial z_i$, $\partial\phi/\partial r_i$, and $\partial q/\partial r_i$ obtained from the differentiation of Eq. (6) are all equal to zero because the boundary values q and ϕ do not depend on the interior point; i.e., $\partial\phi/\partial z_i = \partial\phi/\partial r_i = 0$, $\partial q/\partial z_i = \partial q/\partial r_i = 0$. The derivatives were taken with respect to the base points. The terms q and ϕ that are integrated in (6) are values at the field points (on the boundary of the domain) and are not functions of z_i and r_i of the base points in the interior. Thus, partial derivatives of these terms with respect to interior z 's and r 's will be equal to zero. If the derivatives had been taken with respect to the field points, these terms would not be equal to zero.

In a manner analogous to that employed for the solution on the boundary, S_{kern_z} and D_{kern_z} , and S_{kern_r} and D_{kern_r} can be defined such that:

$$\frac{\partial \phi_i}{\partial z} = \frac{1}{4\pi} \int_{\Gamma} [qS_{\text{kern}_z} - \phi D_{\text{kern}_z}] d\Gamma, \tag{A18}$$

$$\frac{\partial \phi_i}{\partial r} = \frac{1}{4\pi} \int_{\Gamma} [qS_{\text{kern}_r} - \phi D_{\text{kern}_r}] d\Gamma \tag{A19}$$

where

$$D_{\text{kern}_z} = \frac{-2(z - z_i)}{a^{3/2}} A - \frac{2}{\sqrt{a}} (B + C + H), \tag{A20}$$

$$S_{\text{kern}_z} = \frac{16r^2 r_i (z - z_i)}{\sqrt{a^5}} F_1(p) + \frac{4r(z - z_i)K(p)}{\sqrt{a^3}}, \tag{A21}$$

$$D_{\text{kern}_r} = \frac{2(r + r_i)}{\sqrt{a^3}} L - \frac{2}{\sqrt{a}} (M + NO - P), \tag{A22}$$

$$S_{\text{kern}_r} = \frac{-8r[r_i^2 - r^3 - r(z - z_i)^2]}{\sqrt{a^5}} F_1(p) - \frac{4(r + r_i)rK(p)}{\sqrt{a^3}}. \tag{A23}$$

Eqs. (A18) and (A19) are then rewritten as the sum of the integrals along each element. Because ϕ and q are assumed to vary linearly over the length of an element, the values of ϕ and q at any point on a given element bounded by nodes j and $j + 1$ are:

$$\phi = \phi_j \frac{\Gamma_{j+1} - \Gamma}{\Gamma_{j+1} - \Gamma_j} + \phi_{j+1} \frac{\Gamma - \Gamma_j}{\Gamma_{j+1} - \Gamma_j}, \tag{A24}$$

$$q = q_j \frac{\Gamma_{j+1} - \Gamma}{\Gamma_{j+1} - \Gamma_j} + q_{j+1} \frac{\Gamma - \Gamma_j}{\Gamma_{j+1} - \Gamma_j}, \tag{A25}$$

where Γ is the distance of the point of interest from the starting end of the element. If terms I_{1z_r} , I_{2z_r} , I_{3z_r} , and I_{4z_r} are defined so that:

$$I_{1z} = \int_{\Gamma_j}^{\Gamma_{j+1}} \frac{\Gamma_{j+1} - \Gamma}{\Gamma_{j+1} - \Gamma_j} S_{\text{kern}_z} d\Gamma, \tag{A26}$$

$$I_{2z} = \int_{\Gamma_j}^{\Gamma_{j+1}} \frac{\Gamma - \Gamma_j}{\Gamma_{j+1} - \Gamma_j} S_{\text{kern}_z} d\Gamma, \tag{A27}$$

$$I_{3z} = \int_{\Gamma_j}^{\Gamma_{j+1}} \frac{\Gamma_{j+1} - \Gamma}{\Gamma_{j+1} - \Gamma_j} D_{\text{kern}_z} d\Gamma, \tag{A28}$$

$$I_{4z} = \int_{\Gamma_j}^{\Gamma_{j+1}} \frac{\Gamma - \Gamma_j}{\Gamma_{j+1} - \Gamma_j} D_{\text{kern}_z} d\Gamma, \tag{A29}$$

and

$$I_{1r} = \int_{\Gamma_j}^{\Gamma_{j+1}} \frac{\Gamma_{j+1} - \Gamma}{\Gamma_{j+1} - \Gamma_j} S_{\text{kern}_r} d\Gamma, \tag{A30}$$

$$I_{2r} = \int_{\Gamma_j}^{\Gamma_{j+1}} \frac{\Gamma - \Gamma_j}{\Gamma_{j+1} - \Gamma_j} S_{\text{kern}_r} d\Gamma, \tag{A31}$$

$$I_{3r} = \int_{\Gamma_j}^{\Gamma_{j+1}} \frac{\Gamma_{j+1} - \Gamma}{\Gamma_{j+1} - \Gamma_j} D_{\text{kern}_r} d\Gamma, \tag{A32}$$

$$I_{4r} = \int_{\Gamma_j}^{\Gamma_{j+1}} \frac{\Gamma - \Gamma_j}{\Gamma_{j+1} - \Gamma_j} D_{\text{kern}_r} d\Gamma, \tag{A33}$$

and if we divide each of the integrals into two parts, Eqs. (A18) and (A19) become:

$$\begin{aligned} \frac{\partial \phi_i}{\partial z} &= \int_{\Gamma} q_j \frac{\Gamma_{j+1} - \Gamma}{\Gamma_{j+1} - \Gamma_j} S_{\text{kern}_z} d\Gamma + \int_{\Gamma} q_{j+1} \frac{\Gamma - \Gamma_j}{\Gamma_{j+1} - \Gamma_j} S_{\text{kern}_z} d\Gamma \\ &\quad - \int_{\Gamma} \phi_j \frac{\Gamma_{j+1} - \Gamma}{\Gamma_{j+1} - \Gamma_j} D_{\text{kern}_z} d\Gamma - \int_{\Gamma} \phi_{j+1} \frac{\Gamma - \Gamma_j}{\Gamma_{j+1} - \Gamma_j} D_{\text{kern}_z} d\Gamma \\ &= \sum_{j=1}^{n-1} [q_j I_{1(ij)_z} + q_{j+1} I_{2(ij)_z}] - [\phi_j I_{3(ij)_z} + \phi_{j+1} I_{4(ij)_z}], \end{aligned} \tag{A34}$$

$$\begin{aligned} \frac{\partial \phi_i}{\partial r} &= \int_{\Gamma} q_j \frac{\Gamma_{j+1} - \Gamma}{\Gamma_{j+1} - \Gamma_j} S_{\text{kern}_r} d\Gamma + \int_{\Gamma} q_{j+1} \frac{\Gamma - \Gamma_j}{\Gamma_{j+1} - \Gamma_j} S_{\text{kern}_r} d\Gamma \\ &\quad - \int_{\Gamma} \phi_j \frac{\Gamma_{j+1} - \Gamma}{\Gamma_{j+1} - \Gamma_j} D_{\text{kern}_r} d\Gamma - \int_{\Gamma} \phi_{j+1} \frac{\Gamma - \Gamma_j}{\Gamma_{j+1} - \Gamma_j} D_{\text{kern}_r} d\Gamma \\ &= \sum_{j=1}^{n-1} [q_j I_{1(ij)_r} + q_{j+1} I_{2(ij)_r}] - [\phi_j I_{3(ij)_r} + \phi_{j+1} I_{4(ij)_r}], \end{aligned} \tag{A35}$$

The terms $I_{1z_r} - I_{4z_r}$ are calculated using Gaussian quadrature. To use Gaussian quadrature, the limits on the integrations are changed from (Γ_j, Γ_{j+1}) to $(-1, 1)$. This is accomplished with the substitution:

$$\xi = \frac{\Gamma - \bar{\Gamma}}{\frac{\Delta \Gamma_j}{2}}, \tag{A36}$$

where $\bar{\Gamma}$ is the average Γ over the interval. This gives:

$$d\Gamma = \frac{\Delta \Gamma_j}{2} d\xi. \tag{A37}$$

Substituting this into Eqs. (A26)–(A33) reduces them to:

$$I_{1(ij)_z,r} = \frac{\Delta \Gamma_j}{2} \int_{-1}^1 \frac{1 - \xi}{2} S_{\text{kern}_{z,r}}(\xi) d\xi, \tag{A38}$$

$$I_{2(ij)_z,r} = \frac{\Delta \Gamma_j}{2} \int_{-1}^1 \frac{1 + \xi}{2} S_{\text{kern}_{z,r}}(\xi) d\xi, \tag{A39}$$

$$I_{3(ij)_z,r} = \frac{\Delta \Gamma_j}{2} \int_{-1}^1 \frac{1 - \xi}{2} D_{\text{kern}_{z,r}}(\xi) d\xi, \tag{A40}$$

$$I_{4(ij)_z,r} = \frac{\Delta \Gamma_j}{2} \int_{-1}^1 \frac{1 + \xi}{2} D_{\text{kern}_{z,r}}(\xi) d\xi. \tag{A41}$$

References

- Azar, R.G., Yang, Z., Chandra, S., Mostaghimi, J., 2005. Impact of molten metal droplets on the tip of a pin projecting from a flat surface. *Int. J. Heat Fluid Flow* 26, 334–347.
- Aziz, S.D., Chandra, S., 2000. Impact, recoil and splashing of molten metal droplets. *Int. J. Heat Mass Transfer* 43, 2841–2857.
- Blake, T.D., Haynes, J.M., 1969. Kinetics of liquid/liquid displacement. *J. Colloid Interf. Sci.*, 30.
- Bussmann, M., Mostaghimi, J., Chandra, S., 1999. On a three-dimensional volume tracking model of droplet impact. *Phys. Fluids* 11, 1406–1417.
- Bussmann, M., Chandra, S., Mostaghimi, J., 2000. Modeling the splash of a droplet impacting a solid surface. *Phys. Fluids* 12, 3121–3132.
- Chandra, S., Avedisian, C.T., 1991. On the collision of a droplet with a solid surface. *Proc. Royal Soc. London: A* 432, 13–41.
- Cossali, G.E., Coghe, A., Marengo, M., 1997. The impact of a single drop on a wetted solid surface. *Exp. Fluids* 22, 463–472.
- Davidson, M.R., 2000. Boundary integral prediction of the spreading of an inviscid drop impacting on a solid surface. *Chem. Eng. Sci.* 55, 12.
- Davidson, M.R., 2002. Spreading of an inviscid drop impacting on a liquid film. *Chem. Eng. Sci.* 57, 3639–3647.
- Fukai, J., Zhao, Z., Poulikakos, D., Megaridi, C.M., Miyatake, O., 1993. Modeling of the deformation of a liquid droplet impinging upon a flat surface. *Phys. Fluids A* 5, 12.
- Fukai, J., Shiiba, Y., Yamamoto, T., Miyatake, O., Poulikakos, D., Megaridis, C.M., Zhao, Z., 1995. Wetting effects on the spreading of a liquid droplet colliding with a flat surface: experiment and modeling. *Phys. Fluids* 7, 236–247.
- Ge, Y., Fan, L.S., 2005. Three-dimensional simulation of impingement of a liquid droplet on a flat surface in the Leidenfrost regime. *Phys. Fluids* 17, 027104–027120.

- Gong, S.C., 2005. Spreading of droplets impacting on smooth solid surface. *Jpn. J. Appl. Phys.* 44, 2.
- Haller, K.K., Ventikos, Y., Poulidakos, D., 2002. Computational study of high-speed liquid droplet impact. *J. Appl. Phys.* 92, 2821–2828.
- Heister, S.D., 1997. Boundary element methods for two-fluid free surface flows. *Eng. Anal. Boundary Elem.* 19, 9.
- Hilbing, J.H., 1996. Nonlinear modeling of atomization processes. Mechanical Engineering, Purdue University, Lafayette.
- Hoffman, R., 1975. A study of the advancing interface. *J. Colloid Interf. Sci.* 50, 228–241.
- Hung, R.J., Lee, C.C., 1994. Effect of a baffle on slosh waves excited by gravity-gradient acceleration in microgravity. *J. Spacecraft Rockets* 31, 1107–1114.
- Jiang, T.S., Oh, S.G., Slattery, J.C., 1979. Correlation for dynamic contact angle. *J. Colloid Interf. Sci.* 69, 74–77.
- Josserand, C., Zaleski, S., 2003. Droplet splashing on a thin liquid film. *Phys. Fluids* 15, 1650–1657.
- Josserand, C., Lemoyne, L., Troeger, R., Zaleski, S., 2005. Droplet impact on a dry surface: triggering the splash with a small obstacle. *J. Fluid Mech.* 524, 47–56.
- Liu, J., Vu, H., Yoon, S.S., Jepsen, R., Aguilar, G., 2010. Splashing phenomena during liquid droplet impact. *Atomization Sprays* 20, 297–310.
- Mandre, S., Mani, M., Brenner, M.P., 2009. Precursors to splashing of liquid droplets on a solid surface. *Phys. Rev. Lett.* 102, 134502, 134501–134504.
- Mani, M., Mandre, S., Brenner, M.P., 2010. Events before droplet splashing on a solid surface. *J. Fluid Mech.* 647, 163–185.
- Mao, T., Kuhn, C.S., Tran, H., 1997. Spread and rebound of liquid droplets upon impact on flat surfaces. *AIChE J.* 43, 11.
- Mehdi-Nejad, V., Mostaghimi, J., Chandra, S., 2003. Air bubble entrapment under an impacting droplet. *Phys. Fluids* 15, 173–183.
- Mukherjee, S., Abraham, J., 2007. Investigations of drop impact on dry walls with a lattice-Boltzmann model. *J. Colloid Interf. Sci.* 312, 341–354.
- Mundo, C., Sommerfeld, M., Tropea, C., 1995. Droplet-wall collisions: experimental studies of the deformation and breakup process. *Int. J. Multiphase Flow* 21, 151–173.
- Oguz, H.N., Prosperetti, A., 1990. Bubble entrainment by the impact of drops on liquid surfaces. *J. Fluid Mech.* 219, 143–179.
- Park, H., Yoon, S.S., Jepsen, R.A., Heister, S.D., Kim, H.Y., 2008. Droplet bounce simulations and air pressure effects on the deformation of pre-impact droplets, using a boundary element method. *Eng. Anal. Boundary Elem.* 32, 21–31.
- Pasandideh-Fard, M., Qiao, Y.M., Chandra, S., Mostaghimi, J., 1996. Capillary effects during droplet impact on a solid surface. *Phys. Fluids A* 8, 10.
- Ponstein, J., 1959. Instability of rotating cylindrical jets. *Appl. Sci. Res.* 8, 425–456.
- Qian, J., Law, C.K., 1997. Regimes of coalescence and separation in droplet collision. *J. Fluid Mech.* 331, 59–80.
- Ranabothu, S.R., Karnezis, C., Dai, L.L., 2005. Dynamic wetting: hydrodynamic or molecular-kinetic? *J. Colloid Interf. Sci.* 288, 213–221.
- Reiber, M., Frohn, A., 1999. A numerical study on the mechanism of splashing. *Int. J. Heat Fluid Flow* 20, 455–461.
- Rein, M., Delplanque, J.-P., 2008. The role of air entrainment on the outcome of drop impact on a solid surface. *Acta Mech.* 201, 105–118.
- Renardy, Y.Y., Popinet, S., Duchemin, L., Renardy, M., Zaleski, S., Josserand, C., Drumright-Clarke, M.A., Richard, D., Clanet, C., Quere, D., 2003. Pyramidal and toroidal water drops after impact on a solid surface. *J. Fluid Mech.* 484, 15.
- Reznik, S.N., Yarin, A.L., 2002. Spreading of a viscous drop due to gravity and capillarity on a horizontal or an inclined dry wall. *Phys. Fluids* 14, 118–132.
- Sato, K., Tomita, Y., Shima, A., 1994. Numerical analysis of a gas bubble near a rigid boundary in an oscillatory pressure field. *J. Acoust. Soc. Am.* 95, 2416–2424.
- Schneemilch, M., Hayes, R.A., Petrov, J.G., Ralston, J., 1998. Dynamic wetting and dewetting of a low-energy surface by pure liquids. *Langmuir* 14, 7047–7051.
- Seebergh, J.E., Berg, J.C., 1992. Dynamic wetting in the low capillary number regime. *Chem. Eng. Sci.* 47, 4455–4464.
- Sikalo, S., Wilhelm, H.D., Roisman, I.V., Jakirlic, S., Tropea, C., 2005. Dynamic contact angle of spreading droplets: experiments and simulations. *Phys. Fluids* 17, 062103.
- Spangler, C.A., Hilbing, J.H., Heister, S.D., 1995. Nonlinear modeling of jet atomization in the wind-induced regime. *Phys. Fluids* 7, 8.
- Stow, C.D., Hadfield, M.G., 1981. An experimental investigation of fluid flow resulting from the impact of a water drop with an unyielding dry surface. *Proc. Royal Soc. London: A* 373, 419–441.
- Trapaga, G., Szekely, J., 1991. Mathematical modeling of the isothermal impingement of liquid droplets in spraying processes. *Metall. Trans. B* 22, 14.
- Wang, Q.X., Yeo, K.S., Khoo, B.C., Lam, K.Y., 1996. Nonlinear interaction between gas bubble and free surface. *Comput. Fluids* 25, 607–628.
- Wang, Q.X., Yeo, K.S., Khoo, B.C., Lam, K.Y., 2005. Vortex ring modeling of toroidal bubbles. *Theor. Comput. Fluid Dyn.* 19, 303–317.
- Weiss, D.A., Yarin, A.L., 1999. Single drop impact onto liquid films: neck distortion, jetting, tiny bubble entrainment, and crown formation. *J. Fluid Mech.* 385, 229–254.
- Worthington, A.M., 1876. On the forms assumed by drops of liquids falling vertically on a horizontal plate. *Proc. Royal Soc. London: A* 25, 11.
- Worthington, A.M., 1877. A second paper on the forms assumed by drops of liquids falling vertically on a horizontal plate. *Proc. Royal Soc. London: A* 25, 6.
- Worthington, A.M., 1908. A Study of Splashes. Longmans, London, United Kingdom.
- Xu, L., 2007. Liquid drop splashing on smooth, rough, and textured surfaces. *Phys. Rev. E* 75, 056316.
- Xu, L., Zhang, W.W., Nagel, S.R., 2005. Drop splashing on a dry smooth surface. *Phys. Rev. Lett.* 94, 184505–184508.
- Yarin, A.L., Weiss, D.A., 1995. Impact of drops on solid surfaces: self-similar capillary waves, and splashing as a new type of kinematic discontinuity. *J. Fluid Mech.* 283, 141–173.
- Yokoi, K., Vadillo, D., Hinch, J., Hutchings, I., 2009. Numerical studies of the influence of the dynamic contact angle on a droplet impacting on a dry surface. *Phys. Fluids* 21, 072102.
- Yoon, S.S., Heister, S.D., 2004. A fully nonlinear model for atomization of high-speed jets. *Eng. Anal. Boundary Elem.* 28, 13.
- Yoon, S.S., Jepsen, R.A., Nissen, M.R., O'Hern, T.J., 2007. Experimental investigation on splashing and nonlinear fingerlike instability of large water drops. *J. Fluids Struct.* 23, 101–115.
- Yoon, S.S., Jepsen, R.A., James, S.C., Liu, J., Aguilar, G., 2009a. Are drop-impact phenomena described by Rayleigh–Taylor or Kelvin–Helmholtz theory? *Drying Technol.*, 27.
- Yoon, S.S., Kim, H.Y., Lee, D., Kim, N., Jepsen, R.A., James, S.C., 2009b. Experimental splash studies of monodisperse sprays impacting variously shaped surfaces. *Drying Technol.* 27, 258–266.